



Published in final edited form as:

*Neuroinformatics*. 2019 January ; 17(1): 131–145. doi:10.1007/s12021-018-9391-z.

## A Web-Based Atlas Combining MRI and Histology of the Squirrel Monkey Brain

Kurt Schilling, Yurui Gao, Matthew Christian, Vaibhav Janve, Iwona Stepniewska, Bennett A. Landman, and Adam W. Anderson

### Abstract

The squirrel monkey (*Saimiri sciureus*) is a commonly-used surrogate for humans in biomedical research. In the neuroimaging community, MRI and histological atlases serve as valuable resources for anatomical, physiological, and functional studies of the brain; however, no digital MRI/histology atlas is currently available for the squirrel monkey. This paper describes the construction of a web-based multi-modal atlas of the squirrel monkey brain. The MRI-derived information includes anatomical MRI contrast (i.e., T2-weighted and proton-density-weighted) and diffusion MRI metrics (i.e., fractional anisotropy and mean diffusivity) from data acquired both in vivo and ex vivo on a 9.4 Tesla scanner. The histological images include Nissl and myelin stains, co-registered to the corresponding MRI, allowing identification of cyto- and myelo-architecture. In addition, a bidirectional neuronal tracer, biotinylated dextran amine (BDA) was injected into the primary motor cortex, enabling highly specific identification of regions connected to the injection location. The atlas integrates the results of common image analysis methods including diffusion tensor imaging glyphs, labels of 57 white-matter tracts identified using DTI-tractography, and 18 cortical regions of interest identified from Nissl-revealed cyto-architecture. All data are presented in a common space, and all image types are accessible through a web-based atlas viewer, which allows visualization and interaction of user-selectable contrasts and varying resolutions. By providing an easy to use reference system of anatomical information, our web-accessible multi-contrast atlas forms a rich and convenient resource for comparisons of brain findings across subjects or modalities. The atlas is called the Combined Histology-MRI Integrated Atlas of the Squirrel Monkey (CHIASM). All images are accessible through our web-based viewer (<https://chiasm.vuse.vanderbilt.edu/>), and data are available for download at (<https://www.nitrc.org/projects/smatlas/>).

### Keywords

Web-based atlas; MRI; histology; squirrel monkey; user interactive

### Information Sharing Statement

Combined Histology-MRI Integrated Atlas of the Squirrel Monkey (CHIASM) images are accessible through our web-based viewer: <https://chiasm.vuse.vanderbilt.edu/>. All data are available for download at: <https://www.nitrc.org/projects/smatlas/>.

## 1. Introduction

Non-human primates (NHP) are phylogenetically close to humans, sharing genetic, anatomical, and physiological similarities (Hendrickx and Binkerd 1990), making them a valuable model for biomedical studies of the brain. Numerous white matter pathways, as well as major functional subdivisions of the cortex, have been shown to have homologous counterparts in the human brain. This includes well defined lateral, central, and temporal sulci, as well as parietal, occipital, frontal, and temporal lobes. NHPs have sophisticated behavioral and cognitive capacities, and the use of NHPs allows access to “ground truth” anatomical or microstructural information via post-mortem histology, upon which experiments can be designed and evaluated.

One of the most commonly studied New World primates is the squirrel monkey (*Saimiri sciureus*). In addition to the above, squirrel monkeys have a relatively small, lissencephalic brain, making experimentation less cumbersome, and histological processing easier. Moreover, because of their small size they can be handled easily, trained to perform in behavioral experiments, and have relatively low resource requirements. Studies using the squirrel monkey are prevalent in neuroscience and related fields, including ophthalmology, toxicology, pharmacology, and psychiatry (Merzenich et al. 1983; Roe et al. 2017; Banks et al. 2017; Uno et al. 2016; Secci et al. 2017; Murakami et al. 2014; Myers et al. 2007; Wang et al. 2013; Wu et al. 2016; Chen et al. 2015; Chen et al. 2003; Chen et al. 2017).

Brain atlases are useful for analyzing and identifying neurological structures. Currently, two stereotaxic atlases from the 1960's are available for the squirrel monkey brain (Akert 1963; MacLean 1962). Brain structures in these atlases are delineated based on cyto-architecture in Nissl stained sections and on myelo-architecture in myelin stained sections. However, these are printed atlases and, unlike digital atlases, do not facilitate spatial normalization of new image information for quantitative comparisons of brains across subjects, time, or differing experimental conditions. In other species, atlases based on magnetic resonance imaging (MRI) have become valuable tools to reference the anatomy of the brain (Hsiao et al. 2011; Sunkin et al. 2013; Ding et al. 2017; Woodward et al. 2018; Frey et al. 2011; Toga et al. 1989) (<http://observatory.brain-map.org/visualcoding>, <https://brainknowledge.mricloud.org/map%3Fmapname=wholebrain>, [http://www.thehumanbrain.info/brain/brain\\_navigator.php](http://www.thehumanbrain.info/brain/brain_navigator.php)) Recently, we have introduced the first MRI atlas of the squirrel monkey brain to facilitate three-dimensional (3D) anatomical localization or segmentation, and to enable comparisons of experimental data across different subjects (K. G. Schilling et al. 2017).

While MRI allows for 3D viewing of the brain and specific structures within it, precise spatial relationships between structures and differentiation between types of tissue, the image resolution is somewhat limited. Stained tissue sections, on the other hand, offer high spatial resolution, and the ability to identify individual cells and fiber systems, however, there are often spatial distortions inherent in histological sectioning, staining, and processing. Here, we present a web-based digital atlas of the squirrel monkey brain that combines aligned MRI and histology data. The MRI includes anatomical and diffusion contrasts, and histology includes Nissl and myelin stains. In addition, a bi-directional

(anterograde and retrograde) tracer is injected into the primary motor cortex of the subjects, and histologically processed in order to identify white matter pathways associated with the injection location. All histological contrasts are registered to the corresponding MRI data of the same specimen. The atlas also includes post-processed results, including diffusion tensor imaging glyphs, diffusion tractography-defined white matter labels, and cyto-architecturally defined cortical regions. This atlas is designed to provide an easy-to-use resource for anatomical, functional, and physiological studies of the squirrel monkey brain that may benefit from information gathered through either histological or MRI modalities. Thus, the atlas provides a convenient medium for comparisons of brain findings across subjects or modalities. To highlight typical usage, we also present three illustrations of the application of data contained in this atlas to neuroscience research, with a focus on diffusion MRI fiber tractography. All images are accessible through our web-based atlas viewer (<https://chiasm.vuse.vanderbilt.edu/>).

## 2. Methods and Materials

### 2.1 Data Acquisition Overview

Figure 1 shows an overview of the atlas data acquisition pipeline. Three squirrel monkeys were imaged in at least two in vivo scan sessions. Following scanning, a bidirectional tracer, biotinylated dextran amine (BDA) was injected into the left hemisphere primary motor cortex (M1). One to three weeks after surgery, the monkey was sacrificed. The brain was then removed from the skull and scanned ex vivo. After this session, the brain was frozen and cut serially on a microtome in the coronal plane. For registration purposes, the surface of the frozen tissue block (i.e. the “block face”) was photographed using a digital camera prior to cutting every third section. Next, series of sections were processed for BDA histochemistry, Nissl, and myelin stains. Finally, borders of cortical regions of interest were manually labeled by an expert based on cyto-architecture provided by Nissl stains. Each data acquisition step is described in full detail below.

All animal procedures for this study were approved by the Vanderbilt University Animal Care and Use Committee, and followed guidelines of the National Institutes of Health for the care and use of laboratory animals.

### 2.2 MRI Methods

**Animals**—The full acquisition pipeline (Figure 1) was completed for three subjects (subjects #1–3), while three additional subjects (#4–6) were acquired only after sacrifice and did not undergo in vivo scans or tracer injections. The data used to construct the atlas were acquired as part of a longer-term study validating the biological basis of diffusion MRI, hence additional subjects will be continually added to the database.

**In Vivo Imaging**—All in vivo imaging procedures were performed on a Varian 9.4 T, 21 cm horizontal bore imaging system, using a commercially available two-channel Doty quadrature birdcage volume coil (inner diameter = 85mm). The two (or more) in vivo sessions were separated by at least a 20-day interval. During MRI data acquisition, each monkey was maintained under stable anesthesia (isoflurane 0.5%–1.0%) and mechanically

ventilated (40 respiration cycles/min), with head and body stabilized in an MR compatible frame. Vital signs including heart rate (Nonin), core body temperature (SA Instruments), respiration pattern and EKG (SA Instruments), end tidal CO<sub>2</sub>, and SpO<sub>2</sub> (SurgiVet) were monitored and maintained at normal levels throughout the imaging session. Both structural and diffusion-weighted images were acquired in vivo. Structural images were acquired with a standard T1-weighted gradient echo multi-slice (GEMS) sequence (TR = 404ms, TE = 2.4ms, flip angle = 20°, 630µm isotropic voxels, 64×64×80 matrix, NEX = 1). Diffusion-weighted images were acquired using a pulsed gradient spin echo (PGSE) echo planar imaging (EPI) sequence (TR=5.5s, TE=44ms, 32 gradient directions, 630µm isotropic voxel, 64×64×65 matrix) with a b-value, or diffusion weighting, of 1000 s/mm<sup>2</sup>.

**Ex vivo Imaging**—Four weeks after the second in vivo scan, the monkey was given a lethal dose of barbiturate, and perfused through the heart. All blood was rinsed out with physiological saline (0.9% NaCl) followed by fixative (4% paraformaldehyde). The brain was removed from the skull and stored in buffered saline overnight. Ex vivo imaging was performed on the same Varian 9.4 T magnet and also included both structural and diffusion-weighted contrasts. Structural contrasts were acquired with a GEMS sequence with full brain coverage (TR = 963ms, TE = 4ms, flip angle = 20°, 300µm isotropic voxels, 192×128×115 matrix, NEX = 1). Diffusion weighted scans were performed using a PGSE multi-shot spin-warp imaging sequence with the same FOV as the structural images (TR=4.6s, TE=42ms, 32 gradient directions, b≈1000s/mm<sup>2</sup>, 300µm voxel, 192×128×115 matrix).

A slightly different protocol was followed for the three additional subjects (subjects #4–6) that were acquired only after sacrifice (and hence did not have in vivo scans). These brains were also perfusion fixed with 4% paraformaldehyde preceded by rinse with physiological saline. Brains were then removed and immersed for 3 weeks in phosphate-buffered saline (PBS) medium with 1mM Gd-DTPA in order to reduce longitudinal relaxation times (D'Arceuil et al. 2007). The brains were then placed in liquid Fomblin (California Vacuum Technology) prior to scanning. For these specimens, structural imaging was performed using a 3D gradient echo (GE3D) sequence (TR = 50ms; TE = 3ms; flip angle = 45°, NEX = 1) at 200µm isotropic resolution. Diffusion data were acquired using a 3D spin-echo multi-shot diffusion weighted EPI sequence (TR = 410ms; TE = 41ms; NSHOTS = 4; NEX = 1; Partial Fourier k-space coverage = 0.75) at 300µm isotropic resolution. Diffusion gradient duration and separation were 8ms and 22ms, respectively, and 101 diffusion weighted images with uniformly spaced directions were acquired at b-values 3,000, 6,000, 9,000, and 12,000 s/mm<sup>2</sup>. Use of increased numbers of DWIs and larger diffusion weightings allows advanced diffusion processing techniques that require more directions and/or b values than common DTI.

**MRI data processing**—Diffusion MRI pre-processing was performed in the coordinate system the data were acquired in. Steps included correction for movement, susceptibility induced distortions, and eddy currents using FSL's *topup* and *eddy* algorithms (Andersson et al. 2003). The gradient tables were rotated based on the transformations obtained from the corrections. Next, for web visualization, processing is performed in “block-space” (see

Section 2.4, Atlas Framework, Registration), although the registration procedure allows data to be moved to any space (i.e. histology, block, or MR-space) for comparison or overlay between modalities. Diffusion tensors were calculated using weighted-linear least squares fitting, from which maps of mean diffusivity (MD), fractional anisotropy (FA), and diffusion-encoded color-maps were computed. Tensor results are visualized as ellipsoidal glyphs, representing the proton displacement isosurfaces. Constrained spherical deconvolution (CSD) was performed for the high angular resolution datasets (monkeys 4–6) using MRTrix software (Tournier et al. 2012). CSD results are visualized as glyphs representing the estimated fiber orientation distributions. Finally, structural contrasts for all monkeys are also visualized in block-space.

**White Matter Labels**—The atlas contains individual white matter labels for three monkeys (#1–3), based on processed ex vivo diffusion weighted images using diffusion fiber tractography (Mori et al. 1999). Detailed procedures are described in (Gao et al. 2016). Due to structural similarities between the macaque and squirrel monkey brain, the results of a comprehensive set of histological tracer injections of the macaque brain, described in (Schmahmann and Pandya 2009), were used as a reference for both seeding and refining tracts. Deterministic fiber tractography, and subsequent tract trimming and editing, were performed in DSI Studio (Yeh et al. 2013). Tracking parameters (including FA threshold, step size, angular threshold) were manually tuned according to the characteristics of each white matter bundle. All 3D fiber tracts were stored as tract density maps, and thresholded, resulting in a binary mask for each white matter pathway. All white matter pathways were checked by a neuroanatomist with expertise in nonhuman primate brain structure, assessing the coarse shape and orientation of each tract, the gray matter structures next to each bundle, and the cortical regions connected by the pathways. This procedure resulted in 57 white matter labels for each monkey. The full set of white matter labels is listed in Table 1.

### 2.3 Histology methods

**Tracer Injection**—BDA is a commonly utilized neuroanatomical tracer for studying neural pathways. Because it can be transported both anterograde and retrograde, BDA can yield sensitive and detailed labeling of both axons and terminals, as well as neuronal cell bodies (Reiner et al. 2000). This tracer relies on axonal transport systems; thus, BDA injection is performed prior to ex vivo scanning (see Figure 1). Under general anesthesia using aseptic techniques, BDA (Molecular Probes Inc., Eugene, OR) was injected (as a 10% solution in phosphate buffer) into left hemisphere M1 cortex of three monkeys (subjects #1–3). Surgical, microstimulation, and injection procedures followed those in previous studies (Stepniewska et al. 1993; Gao et al. 2013). Pressure injections of BDA were carried out using a 2 ul Hamilton syringe. Eight injections (1 ml/ site) were made in order to cover a large M1 region representing the forearm as identified by intracortical microstimulation. After each injection, the needle was left in the brain for 5–10 minutes and then retracted stepwise to avoid leakage of the tracer along the needle track. After surgery, the monkey was allowed to recover, giving the tracer sufficient time to be transported along axons to all regions connected to M1.

**Histological Acquisition**—Following ex vivo MRI scanning, the brain was frozen and cut serially on a manually operated frozen microtome in the coronal plane at 50  $\mu\text{m}$  thickness. All sections were collected in phosphate buffer, but prior to cutting every third section (i.e., at 150  $\mu\text{m}$  intervals), the surface of the frozen tissue block was photographed using a Canon digital camera (image resolution = 50  $\mu\text{m}/\text{pixel}$ , image size = 3330 $\times$ 4000 pixels, number of images per brain ~ 280), mounted above the microtome. These block-face images have been shown to produce more robust inter-modality registration results by providing a relatively undistorted intermediate reference space between the histological and MRI data (Toga et al. 1994).

Three stains were performed for each brain. A cresyl violet Nissl stain (Paul et al. 2008) for identification of cell bodies, a Gallyas silver stain (Gallyas 1971) to identify myelinated axons, and processing for BDA (Reiner et al. 2000) to trace pathways associated with M1 cortex. Sections were divided into six series, and every sixth tissue section was processed for a given stain (for example sections #1, 7, 13 for Nissl). To summarize, MRI resolution is 300 $\mu\text{m}$ , block-face resolution is 150 $\mu\text{m}$ , tissue section thickness is 50 $\mu\text{m}$  and each stain is performed every 6<sup>th</sup> slice, resulting in each stain having a “resolution” of approximately 300 $\mu\text{m}$ .

Whole-slide brightfield microscopy was performed using a Leica SCN400 Slide Scanner at 20 $\times$  magnification, resulting in a maximum in-plane resolution of 0.5 $\mu\text{m}/\text{pixel}$ . The images are stored in the Leica image file format (file extension: SCN), which stores a hierarchical series of images at varying resolution levels. Each series has the associated size, position, and resolution, as well as the image data stored as TIFF data. For example, there are five levels, ranging from level #0 at 0.5  $\mu\text{m}/\text{pixel}$  (typical size ~80,000 $\times$ 80,000 pixels) to level #4, down-sampled by a factor of 256 to a resolution of 128  $\mu\text{m}/\text{pixel}$  (typical size ~300 $\times$ 300 pixels).

**Cortical Labels**—The atlas contains cortical labels for three monkey brains (#1–3), that were histologically defined based on cytoarchitectural features revealed in Nissl-stained sections. Eighteen cortical regions of interest (ROIs) in the frontal and parietal lobes were identified in Nissl stained sections by an experienced neuroanatomist and areal borders were manually labeled on the digitized images of these sections. Boundaries between cortical areas were marked based on cytoarchitectural features such as of cell density, cell sizes, and thickness of the cortex and cortical layers. The regions chosen represent a common parcellation of the non-human primate cortex (Kaas et al. 2012; Preuss et al. 1996; Stepniewska et al. 1993; Kaas 2005; Kaas et al. 2011), with a focus on regions connected to the primary motor area. Since these brains received BDA injections in M1, borders seen in Nissl sections were confirmed by the distribution of BDA labeled neurons (e.g. PMC-PFC border was distinguished by the presence of BDA labelled cells in PMC, but not in PFC). In contrast to motor-connected areas, the primary visual cortex (V1) was easily distinguished in Nissl stained sections due to its prominent inner granular layer 4 with very high neuronal density and thick band of myelinated axons that run parallel to the surface (stria of Gennari). Labelling was performed using ITK-SNAP (Version 2.4.0), and labels were digitized to create masks for each ROI. The full set of cortical labels is listed in Table 1.



## 2.4 Atlas Framework

In order to transfer information between high-resolution microscopy and MRI data, a multi-step registration scheme was utilized. Figure 2 summarizes the steps of this procedure. The aim is to provide an atlas framework which facilitates comparisons across modalities.

**Registration**—The multi-step registration utilized here is very similar to the registration procedure validated in an earlier study (Choe et al. 2011), which showed that the accuracy of the overall registration was approximately one MRI voxel (~0.3mm). From the Leica image file, the TIFF image stored at 128um/pixel (down-sample factor 256) was extracted and registered to the down-sampled photograph (256×256 pixels at a resolution of approximately 128um/pixel) of the corresponding tissue block using a 2D affine transformation followed by a 2D non-rigid transformation, semi-automatically calculated via the Thin-Plate Spline algorithm (Bookstein 1989). Next, all down-sampled block face photographs were assembled into a 3D block volume and registered to the corresponding 3D MRI volume using a 3D affine transformation followed by a non-rigid transformation automatically calculated via the Adaptive Bases Algorithm (Rohde et al. 2003) (AMIR-Automatic Manual Information based affine image Registration, 2003, used for affine transforms, and SPLINE algorithm, 2003, for non-rigid deformations). The deformation fields produced by all registration steps are saved in order to transfer any set of acquired data (or processed data) to any desired space for comparisons.

For the web-interface, we have chosen to display all data (high resolution histology, block-face photographs, in vivo and ex vivo MRI) in the intermediate block-space.

**Layer construction**—As described above, the histology images are captured at a resolution of 0.5um/pixel. For comparisons of high-resolution histology with MRI images that have fields-of-view on the order of tens-of-millimeters (for example ~40 mm), the histology file would contain billions of pixels (~80,000×80,000 pixels), making the image much larger than is reasonably handled in a browser viewport, and hindering interactive panning or zooming functions. For this reason, all images are “tiled”, or “shredded” into smaller PNG files (on the order of ~256×256 pixels) which are dynamically loaded and stitched together for viewing (see Web Viewer Tool section for details). In this way, the user can assess the data at a resolution suitable for the task at hand, loading and manipulating millions of pixels rather than billions. The tiling and viewing in this manuscript is an extension of the logic developed in an earlier work (Sun et al. 2015).

All histological images were tiled in block-space, and in the coronal plane. For histological level #4, the OpenSlide (Goode et al. 2013) library (a C-based library for whole-slide digital images) was used to read and extract the corresponding image matrix from the SCN file, and the image was deformed to block-space using the appropriate 2D deformation field. Finally, the 256×256 image was saved as a PNG file. For higher-resolution levels (levels #3 through #0), the deformation field was up-sampled to the appropriate spatial resolution, the corresponding image matrix was read from the SCN file, and the deformation field was applied to this image. The final histological images (now in block-space) were saved as a series of 256×256 PNGs covering the entire field-of-view. For example, level #3 contains 16

PNGs (four rows by four columns), while level #0 (at 0.5um/pixel) contains 65,536 PNGs (256 rows by 256 columns). This procedure was repeated for every slice in block space. Finally, all PNGs were stored on a CentOS 7 web-server, and a Postgres database created to store meta-information about image locations and spatial positions.

Similar tiling was performed for MRI and block-face data. Because these are not acquired at high resolution, they are saved as PNGs at the resolution of the block-face image only, corresponding to histology level #4. In addition to coronal images, these two modalities are also tiled in axial and sagittal views to facilitate 3D localization and visualization.

**Web Viewer Tool**—The web interface aims to support exploring the squirrel monkey brain through both MRI and histological imaging modalities, as well as the relationship between them. Functionality includes the ability to page through MRI volumes in coronal, axial, and sagittal orientations, with cross-hairs showing the 3D position in the brain, displayed with a tri-planar viewer. Drop-down menus allow navigation through different contrasts, sessions, and subjects. Overlays include DTI and CSD diffusion glyphs, as well as both white matter and gray matter labels.

On the histological side, the website displays slices, and facilitates navigating across slices with a slider, as well as scrolling or panning across a slice. Zooming can be performed through sliders and mouse functionality, with a mini-map utilized to display current screen position in the image. Again, drop-down menus allow navigation through different staining contrasts.

Finally, registration of the histology and MRI data supports overlays between the aligned modalities, showing the differing contrasts in the same parts of the same brain. Histology can be overlaid on MRI contrast, with the ability to switch between the various contrasts, as well as change the transparency of the histology modality.

The web viewer is a Python Flask web server that uses PostgreSQL to access the database of images. The web frontend uses HTML5 and the javascript library AngularJS and makes requests to the web server in order to dynamically retrieve images. Specifically, the frontend requests information in the form of JSON text data (image size, number of slices, etc.) and uses this information to form a URL to a specific image on the web-server. The images are rendered using WebGL, including the histology mosaic and the different MR contrasts. When zooming, the frontend uses the magnification factor to determine which histological level to load, and interpolates the images until the magnification reaches the next highest histological level.

All data, including tiled images, processed and unprocessed histology and MRI, block-face images, and deformation fields, are made available at (<https://www.nitrc.org/projects/smatlas/>). The back-end currently includes upwards of 1.2TB of data.

## 2.5 Additional content

Additional content was added to the atlas web-viewer in the form of the VALiDATE29 multi-channel atlas of the squirrel monkey brain (K. G. Schilling et al. 2017). This atlas is based



on multiple types of MRI contrast acquired on 29 squirrel monkeys, and created using nonlinear registration techniques, resulting in a population-averaged stereotaxic coordinate system. The coordinate system was made to be anatomically similar to that created for human imaging (Mori et al. 2008; Mazziotta et al. 1995), with the midsagittal plane aligned with the mid-plane of the image grid ( $x=0$  plane), the center of the anterior commissure (AC) and posterior commissure (PC) brought into the same oblique-axial plane, and the PC located directly posterior to the AC. The coordinate system was adjusted so that the AC landmark became the origin (0,0,0) of the image coordinate system, with image grid at 0.3mm isotropic resolution.

The MRI-based atlas contains T1, T2, T2\*, and diffusion-weighted MRI templates, as well as population averaged cortical and white matter labels. The atlas facilitates spatial normalization for comparisons of data across subjects or differing experimental conditions, as well as label propagation to identify regions of interest. The VALiDATE29 atlas is presented in the web-viewer in its own space (as opposed to all other data in block-space), in sagittal, coronal, and axial orientations. Functionality includes scrolling, zooming, and panning throughout the atlas-space as well as overlays of labels and differing contrasts. VALiDATE29 data are made available with all other data content (<https://www.nitrc.org/projects/smatlas/>), as well as downloadable separately at <https://www.nitrc.org/projects/validate29/> (K. G. Schilling et al. 2017).

### 3. Results

The squirrel monkey atlas is available at <https://chiasm.vuse.vanderbilt.edu/> and the complete set of images upon which the atlas is based is freely available at (<https://www.nitrc.org/projects/smatlas/>). This includes unprocessed histology and MRI, deformation fields, as well as VALiDATE29 atlas and templates.

#### 3.1 Atlas Contents

All data in the web-viewer are aligned to each subject's block-face images. Figure 3 shows a selection of MRI (top) and histology (bottom) data for a single subject. MRI data for all subjects, all sessions, and all contrasts (both acquired and calculated contrasts) are presented in a tri-planar viewer. Figure 3 (top) shows the mean ex vivo diffusion weighted image, the ex vivo T2 contrast, the in vivo (session 1) T2 contrast, and the in vivo (session 2) processed FA maps for a selected subject, which demonstrates excellent alignment across sessions and across modalities. In addition to these, contrasts of MD, diffusion tensor elements, mean b0 images, radial anisotropy, diffusion weighted images, RGB color maps, and primary eigenvector maps are also available and viewable.

Histological data for each subject are displayed as coronal slices (Figure 3, bottom), and currently include Nissl, Myelin, and BDA contrasts. Again, contrasts demonstrate excellent alignment in most areas of the brain, even at increased levels of magnification.

Additional content includes block space images, as well as all MRI contrasts made available through the VALiDATE29 squirrel monkey atlas (K. G. Schilling et al. 2017). In addition, white matter and gray matter labels, as well as DTI (and CSD) glyphs are viewable,

although these will be utilized most often as overlays on histological or MR modalities (see “Atlas Interface and Functionality”).

### 3.2 Atlas Interface and Functionality

Figure 4 shows the basic atlas interface for visualizing MRI, histology, block face data, and overlays. The subject and session each have their own drop-down menus. The image type is selected using the “Modalities” layer menu. When a modality is selected, the corresponding contrasts are made available for viewing – this is to reduce menu clutter that would result from showing all contrasts at once. For MRI (Figure 4, A), the “Contrasts” menu includes all contrasts from the given session, which can be viewed by clicking in the selection box. The menu below the image display window contains sliders to facilitate both zooming and scrolling through the 3D volume. In addition, a crosshair tool, pan tool, and minimap tool are selectable in the toolbar above the image display, which facilitate navigation and localization within the image volumes.

For histology (Figure 4, B), images are displayed as coronal slices, and the “Contrasts” menu allows choice of histological stain for a given subject and slice. Again, the menu contains a slider for zoom, which allows viewing histology at a range of magnification levels. Zoom can also be controlled through mouse wheel scrolling, with panning controlled by dragging the mouse. By default, the minimap is displayed, which shows the current location and field of view. Finally, the toolbar again allows selection of crosshair and panning tools, as well as the ability to enable/disable the minimap. It is important to note that a given stain does not exist for every coronal slice; if it does not exist, the entire label in the “Contrasts” menu will indicate this by turning red.

Multiple modalities can be displayed simultaneously. For example, any histological stain can be overlaid onto any coronal MRI contrast. Figure 5 (A and B) shows an example overlay of a Nissl-stained histological slice overlaid on an ex vivo FA map. The transparency of each layer can be adjusted using the slider bar (note differences between Figure 5 A and B). In addition, the overlay order can be changed by dragging and dropping the label in the “Contrast” layers menu, with the order of the labels corresponding to the order of the layers.

Finally, various derived maps can be displayed and/or overlaid on images. For example, anatomical labels (Figure 5, C) can be shown in order to identify the region of the brain currently under investigation. The names of the regions of interest will be displayed as the crosshair tool hovers across the image. Finally, DTI glyphs, which highlight the direction of greatest diffusivity, can be shown over both MRI and histology (Figure 5, D). A reduced number of glyphs are shown at lower magnifications in order to reduce the number of image requests to the server.

### 3.3 Applications

The data in this atlas can be utilized for a broad range of neuroscience investigations. Here, we briefly describe three studies which have utilized the data contained in this atlas: (A) validation of fiber tractography, (B) comparison of fiber orientation and DTI measurements, and (C) label propagation for fiber tractography.

Diffusion fiber tractography has become an extremely useful tool to study the central nervous system, with a wide range of research and clinical applications (Johansen-Berg and Behrens 2006; Jeurissen et al. 2017). However, diffusion MRI typically produces low signal-to-noise ratio images, and the reconstruction and tractography process includes a variety of simplifications and assumptions which may affect the accuracy of reconstructed pathways. For humans, we cannot directly investigate the extent that fiber tractography reveals the true anatomical connectivity, however, animal models allow quantitative assessment of the accuracy of tractography. Using the BDA stained histology in this atlas, Gao et al. (Gao et al. 2013) compared DTI tractography to “ground truth” M1-cortical connectivity revealed by the tracers. By segmenting BDA from histological sections and running tractography algorithms directly on the aligned MRI data, comparisons are easily made between the two modalities (Figure 6, A). Doing this, the authors found that DTI tractography of major pathways predicted inter-regional connectivity comparable to the histological connectivity, but was less reliable in measuring voxel-wise connectivity strengths. Future tractography validation studies with these data could investigate newer high angular resolution algorithms, or other tractography methods (Knosche et al. 2015).

Potential problems for fiber tractography algorithms are inaccuracies in estimating voxel-wise orientation information, which is generally assumed to coincide with the directions of neuronal fibers in each voxel. Having a methodology to compare fiber orientations from diffusion data directly with histological data will give insight into the potential limitations and pitfalls of diffusion MRI. To investigate this, Choe et al. (Choe et al. 2012) used a framework similar to that in this atlas in order to compare myelin-stained brain sections directly to the diffusion parameters from registered DTI (Figure 6, B shows similar results based on atlas data). Using a Fourier-based image processing technique to extract myelin orientations, the authors found that the major eigenvector of the tensor aligned well with the underlying myelinated fibers in voxels with highly coherent fibers, and was able to identify regions of complex fiber structures via a reduced FA (see Figure 6, B for examples using atlas data). The myelin data in our atlas could be processed using similar techniques, in combination with the co-aligned MRI data, to validate both DTI and higher order diffusion models.

A final example application of the atlas is in identifying regions of interest. In addition to the web-based label overlays to localize regions of interest on the histology or MRI, these labels can also be propagated to new datasets for comparisons of data across different subjects or across varying experimental conditions (K. G. Schilling et al. 2017; Gao et al. 2016). The atlas labels can be registered to an individual squirrel monkey brain (or vice-versa) and used for delineating regions of interest, or as seeds for fiber tractography. For example, Figure 6C shows fiber tractography performed after labels for the optic tract, inferior occipito-frontal fasciculus, and corpus callosum were registered to a squirrel monkey diffusion dataset, and used as seed regions for tractography.

## 4. Discussion and Conclusion

Here we present the construction of a web-based multi-modal atlas of the squirrel monkey brain, called the Combined Histological-MRI Integrated Atlas of the Squirrel Monkey

(CHIASM). The atlas data include both in vivo and ex vivo MRI scans (including anatomical and diffusion contrasts), tracer injections, and a variety of histological stains. Calculated parameters, including diffusion MRI glyphs and region of interest labels, are also included in the atlas. All data for a given subject are presented in a common space, a framework which facilitates comparisons across imaging modalities. Data from all subjects are accessible through a web-based atlas viewer, which allows visualization and interaction with data, allowing the user to select contrasts, locations, and varying resolutions. This multi-contrast atlas provides a convenient medium for comparisons of neuroanatomical findings across subjects or modalities, for example, validating MRI measurements with histological correlates. The web-viewer is accessible at <https://chiasm.vuse.vanderbilt.edu/>, and the complete set of images upon which the atlas is based are freely available at <https://www.nitrc.org/projects/smatlas/>.

This web-based digital atlas has several advantages over existing printed atlases (Akert 1963; MacLean 1962). First, the two-dimensional nature of the paper atlases make it difficult to pool data across animals because they cannot utilize modern image registration techniques. Also, they do not offer MRI, or connectivity-specific contrasts. The current digital atlas overcomes both limitations, and accommodates both modern image registration techniques and multiple imaging modalities. More importantly, the digital atlas integrates images from different spatial scales, ranging from the order of millimeters (MRI) to that of micrometers (histology). In addition, the digital data facilitates quantitative analysis (see below) of both microstructure (histology) and macrostructure (DTI tractography), and inclusion of new digital images (MRI, CT, PET, etc.).

We envision the use of these resources by both MRI and neuroscience researchers in two main ways: (1) a qualitative exploration of brain data across modalities, and (2) as a basis for quantitative analysis. The web-viewer by itself is largely qualitative. The browsing and exploration tools allow 3D navigation through the detailed atlas of the isolated brain. Thus, it may act as an anatomical reference, providing spatial context for experiments or for descriptions of location and anatomy. Further, quantitative analysis can be performed on the monkeys in this atlas. For example, histological analysis could be done to quantify BDA tracer connections or myelin densities (see Figure 6, A and B) in order to study individual neuroanatomy, or to validate quantitative MRI measures. Researchers interested in the relationship between a particular histological measure and some MRI metric (for example the cell density from Nissl stains and mean diffusivity from diffusion MRI) can download the appropriate data and registration fields for any, or all, monkeys, and make direct comparisons in either histology, block, or MRI-space by applying the appropriate deformations fields.

These data could also be used on new squirrel monkey datasets collected by researchers at other institutions. Specifically, the stereotaxic atlas (VALiDATE29) could be used for spatial normalization and label propagation. In both cases, one would download the atlas, and register the individual brains to the appropriate VALiDATE29 template (for example, a new T1 image to the T1 population averaged template) using a registration algorithm of choice – in addition to that implemented in our study (Rohde et al. 2003), there are several popular open source packages used in the literature (Avants et al. 2011; Jenkinson et al. 2012;

Ashburner 2007; Klein et al. 2010), among others. The resulting deformation could be applied to the new image, and structures of interest (for example, lesions, fMRI activation, injection regions, structural connections) can now be located in the atlas space and given meaningful coordinates, which makes the positioning, visualization, and communication of scientific findings easier. This spatial normalization can also be applied for pooling of data across experiments, across monkeys, or across time. One can also use the resulting deformation field for label propagation. In this case, the atlas segmentation can be propagated to the new individual using the derived deformation fields, resulting in automatic anatomical segmentation and tissue classification (i.e. white versus gray matter). Finally, the stereotaxic atlas could serve as a tool for surgical procedures that use a physical frame around the head, or possibly in conjunction with neuro-navigation software. For example, we aim to make future injections in cerebellar regions of interest. To do this, we will use the procedures described above to determine the location of our intended injection sites in the coronal, sagittal, and axial planes, and modify the physical frame to ensure the syringe is positioned at the correct coordinates.

Future work will include more comprehensive MRI protocols on a larger set of animals, both in vivo and ex vivo. Larger b-values and more diffusion directions will facilitate implementation and validation of a larger selection of high angular resolution diffusion techniques (Dyrby et al. 2011). In addition, multiple MRI modalities can be incorporated, including BOLD contrast, susceptibility imaging, or myelin volume fraction imaging. For histology, more stains will be included, for example acetylcholinesterase to facilitate identifying thalamic nuclei (Stepniewska et al. 1993). In addition to wide-field light microscopy, high resolution 3D confocal images can be included to facilitate comparisons of fiber orientation information estimated from diffusion MRI (K. Schilling et al. 2016). Also, new forms of processed data, including fiber orientation maps (Budde and Annese 2013) or quantified BDA tracer densities, should be included in future iterations of the atlas. We envision future versions of this atlas to be used directly for quantitative analysis and data extraction. Currently, researchers must download data separately from visualization. We aim to eventually make the viewer a direct access point to the data, where a given field of view, resolution, and contrast can be extracted directly from the website and downloaded as a package. In addition, text annotation could be useful for discussion and reporting of results. It would also be useful to link the non-stereotaxic presentation of individuals (currently presented in the individual's block space) to the stereotaxic perspective.

## Acknowledgements

This work was supported by the National Institute of Neurological Disorders and Stroke of the National Institutes of Health under award numbers RO1 NS058639 and S10 RR17799. Whole slide imaging was performed in the Digital Histology Shared Resource at Vanderbilt University Medical Center ([www.mc.vanderbilt.edu/dhsr](http://www.mc.vanderbilt.edu/dhsr)).

## References

- Akert REK (1963). Stereotaxic Atlas of the Brain of the Squirrel Monkey: University of Wisconsin Press.
- Andersson JL, Skare S, & Ashburner J (2003). How to correct susceptibility distortions in spin-echo echo-planar images: application to diffusion tensor imaging. *Neuroimage*, 20(2), 870–888, doi: 10.1016/S1053-8119(03)00336-7. [PubMed: 14568458]

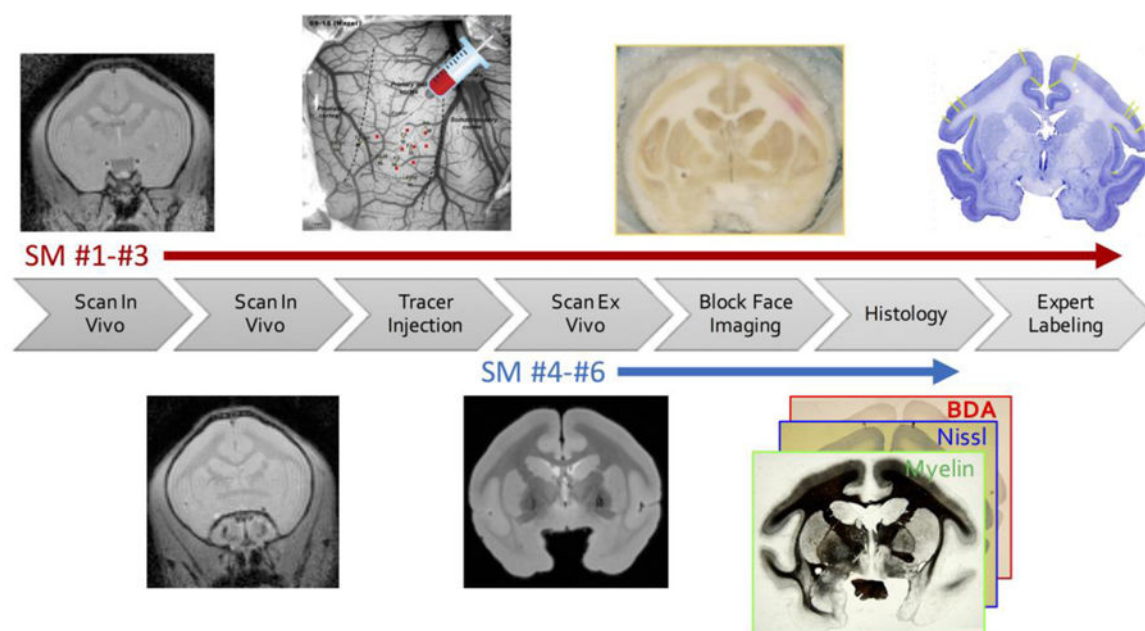
- Ashburner J (2007). A fast diffeomorphic image registration algorithm. *Neuroimage*, 38(1), 95–113, doi:10.1016/j.neuroimage.2007.07.007. [PubMed: 17761438]
- Avants BB, Tustison NJ, Song G, Cook PA, Klein A, & Gee JC (2011). A reproducible evaluation of ANTs similarity metric performance in brain image registration. *Neuroimage*, 54(3), 2033–2044, doi:10.1016/j.neuroimage.2010.09.025. [PubMed: 20851191]
- Banks ML, Czoty PW, & Negus SS (2017). Utility of Nonhuman Primates in Substance Use Disorders Research. *ILAR J*, 1–14, doi:10.1093/ilar/ilx014. [PubMed: 28586416]
- Bookstein FL (1989). Principal Warps - Thin-Plate Splines and the Decomposition of Deformations. *Ieee Transactions on Pattern Analysis and Machine Intelligence*, 11(6), 567–585, doi:10.1109/34.24792.
- Budde MD, & Annese J (2013). Quantification of anisotropy and fiber orientation in human brain histological sections. *Front Integr Neurosci*, 7, 3, doi:10.3389/fnint.2013.00003. [PubMed: 23378830]
- Chen LM, Friedman RM, & Roe AW (2003). Optical imaging of a tactile illusion in area 3b of the primary somatosensory cortex. *Science*, 302(5646), 881–885, doi:10.1126/science.1087846. [PubMed: 14500850]
- Chen LM, Mishra A, Yang PF, Wang F, & Gore JC (2015). Injury alters intrinsic functional connectivity within the primate spinal cord. *Proc Natl Acad Sci U S A*, 112(19), 5991–5996, doi:10.1073/pnas.1424106112. [PubMed: 25902510]
- Chen LM, Yang PF, Wang F, Mishra A, Shi Z, Wu R, et al. (2017). Biophysical and neural basis of resting state functional connectivity: Evidence from non-human primates. *Magn Reson Imaging*, 39, 71–81, doi:10.1016/j.mri.2017.01.020. [PubMed: 28161319]
- Choe AS, Gao Y, Li X, Compton KB, Stepniewska I, & Anderson AW (2011). Accuracy of image registration between MRI and light microscopy in the ex vivo brain. [Research Support, N.I.H., Extramural]. *Magn Reson Imaging*, 29(5), 683–692, doi:10.1016/j.mri.2011.02.022. [PubMed: 21546191]
- Choe AS, Stepniewska I, Colvin DC, Ding Z, & Anderson AW (2012). Validation of diffusion tensor MRI in the central nervous system using light microscopy: quantitative comparison of fiber properties. *NMR Biomed*, 25(7), 900–908, doi:10.1002/nbm.1810. [PubMed: 22246940]
- D’Arceuil HE, Westmoreland S, & de Crespigny AJ (2007). An approach to high resolution diffusion tensor imaging in fixed primate brain. *Neuroimage*, 35 (2), 553–565, doi:10.1016/j.neuroimage.2006.12.028. [PubMed: 17292630]
- Ding SL, Royall JJ, Sunkin SM, Ng L, Facer BA, Lesnar P, et al. (2017). Comprehensive cellular-resolution atlas of the adult human brain. *J Comp Neurol*, 525(2), 407, doi:10.1002/cne.24130. [PubMed: 27917481]
- Dyrby TB, Baare WF, Alexander DC, Jelsing J, Garde E, & Sogaard LV (2011). An ex vivo imaging pipeline for producing high-quality and high-resolution diffusion-weighted imaging datasets. [Research Support, Non-U.S. Gov’t Validation Studies]. *Hum Brain Mapp*, 32(4), 544–563, doi:10.1002/hbm.21043. [PubMed: 20945352]
- Frey S, Pandya DN, Chakravarty MM, Bailey L, Petrides M, & Collins DL (2011). An MRI based average macaque monkey stereotaxic atlas and space (MNI monkey space). *Neuroimage*, 55(4), 1435–1442, doi:10.1016/j.neuroimage.2011.01.040. [PubMed: 21256229]
- Gallyas F (1971). Silver staining of Alzheimer’s neurofibrillary changes by means of physical development. *Acta Morphol Acad Sci Hung*, 19(1), 1–8. [PubMed: 4107507]
- Gao Y, Choe AS, Stepniewska I, Li X, Avison MJ, & Anderson AW (2013). Validation of DTI tractography-based measures of primary motor area connectivity in the squirrel monkey brain. [Research Support, N.I.H., Extramural Validation Studies]. *PLoS One*, 8(10), e75065, doi:10.1371/journal.pone.0075065. [PubMed: 24098365]
- Gao Y, Parvathaneni P, Schilling K, Zu Z, Choe A, Stepniewska I, et al. (2016). A 3D high resolution ex vivo white matter atlas of the common squirrel monkey (*Saimiri sciureus*) based on diffusion tensor imaging. Paper presented at the In Proceedings of the SPIE Medical Imaging Conference, San Diego, California, February



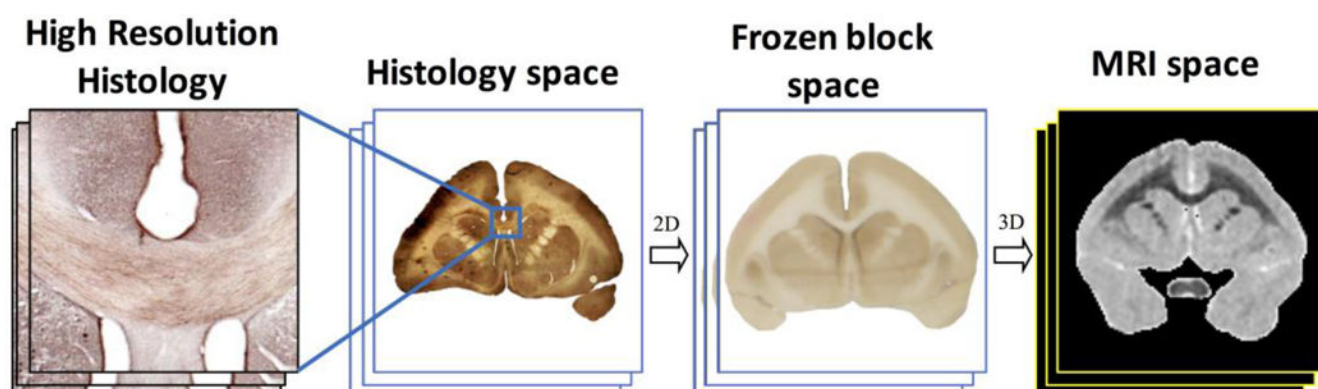
- Goode A, Gilbert B, Harkes J, Jukic D, & Satyanarayanan M (2013). OpenSlide: A vendor-neutral software foundation for digital pathology. *J Pathol Inform*, 4, 27, doi:10.4103/2153-3539.119005. [PubMed: 24244884]
- Hendrickx AG, & Binkerd PE (1990). Nonhuman primates and teratological research. *J Med Primatol*, 19(2), 81–108. [PubMed: 2187096]
- Hsiao MY, Chen CC, & Chen JH (2011). BrainKnowledge: a human brain function mapping knowledge-base system. *Neuroinformatics*, 9(1), 21–38, doi:10.1007/s12021-010-9083-9. [PubMed: 20857233]
- Jenkinson M, Beckmann CF, Behrens TE, Woolrich MW, & Smith SM (2012). Fsl. *Neuroimage*, 62(2), 782–790, doi:10.1016/j.neuroimage.2011.09.015. [PubMed: 21979382]
- Jeurissen B, Descoteaux M, Mori S, & Leemans A (2017). Diffusion MRI fiber tractography of the brain. *NMR Biomed*, doi:10.1002/nbm.3785.
- Johansen-Berg H, & Behrens TE (2006). Just pretty pictures? What diffusion tractography can add in clinical neuroscience. *Curr Opin Neurol*, 19(4), 379–385, doi:10.1097/01.wco.0000236618.82086.01. [PubMed: 16914977]
- Kaas JH (2005). The future of mapping sensory cortex in primates: three of many remaining issues. *Philos Trans R Soc Lond B Biol Sci*, 360(1456), 653–664, doi:10.1098/rstb.2005.1624. [PubMed: 15937006]
- Kaas JH, Gharbawie OA, & Stepniewska I (2011). The organization and evolution of dorsal stream multisensory motor pathways in primates. *Front Neuroanat*, 5, 34, doi:10.3389/fnana.2011.00034. [PubMed: 21716641]
- Kaas JH, Stepniewska I, & Gharbawie O (2012). Cortical networks subserving upper limb movements in primates. *Eur J Phys Rehabil Med*, 48(2), 299–306. [PubMed: 22407009]
- Klein S, Staring M, Murphy K, Viergever MA, & Pluim JP (2010). elastix: a toolbox for intensity-based medical image registration. *IEEE Trans Med Imaging*, 29(1), 196–205, doi:10.1109/TMI.2009.2035616. [PubMed: 19923044]
- Knosche TR, Anwender A, Liptrot M, & Dyrby TB (2015). Validation of tractography: Comparison with manganese tracing. *Hum Brain Mapp*, 36(10), 4116–4134, doi:10.1002/hbm.22902. [PubMed: 26178765]
- MacLean JAGPD (1962). A Stereotaxic Atlas of the Squirrel Monkey's Brain (*Saimiri sciureus*) U.S. Department of Health, Education, and Welfare.
- Mazziotta JC, Toga AW, Evans A, Fox P, & Lancaster J (1995). A probabilistic atlas of the human brain: theory and rationale for its development. The International Consortium for Brain Mapping (ICBM). *Neuroimage*, 2(2), 89–101. [PubMed: 9343592]
- Merzenich MM, Kaas JH, Wall J, Nelson RJ, Sur M, & Felleman D (1983). Topographic reorganization of somatosensory cortical areas 3b and 1 in adult monkeys following restricted deafferentation. *Neuroscience*, 8(1), 33–55. [PubMed: 6835522]
- Mori S, Crain BJ, Chacko VP, & van Zijl PC (1999). Three-dimensional tracking of axonal projections in the brain by magnetic resonance imaging. *Ann Neurol*, 45(2), 265–269. [PubMed: 9989633]
- Mori S, Oishi K, Jiang H, Jiang L, Li X, Akhter K, et al. (2008). Stereotaxic white matter atlas based on diffusion tensor imaging in an ICBM template. *Neuroimage*, 40(2), 570–582, doi:10.1016/j.neuroimage.2007.12.035. [PubMed: 18255316]
- Murakami T, Ibi K, Kuraishi T, Hattori S, Kai C, Ishiguro N, et al. (2014). Failure of heterogeneous amyloid-enhancing factor in geriatric squirrel monkeys (*Saimiri boliviensis*). *J Med Primatol*, 43(6), 488–491, doi:10.1111/jmp.12136. [PubMed: 25041324]
- Myers RM, Greiner SM, Harvey ME, Griesmann G, Kuffel MJ, Buhrow SA, et al. (2007). Preclinical pharmacology and toxicology of intravenous MV-NIS, an oncolytic measles virus administered with or without cyclophosphamide. *Clin Pharmacol Ther*, 82(6), 700–710, doi:10.1038/sj.clpt.6100409. [PubMed: 17971816]
- Paul CA, Beltz B, & Berger-Sweeney J (2008). The nissl stain: a stain for cell bodies in brain sections. *CSH Protoc*, 2008, pdb prot4805, doi:10.1101/pdb.prot4805.
- Preuss TM, Stepniewska I, & Kaas JH (1996). Movement representation in the dorsal and ventral premotor areas of owl monkeys: a microstimulation study. *J Comp Neurol*, 371(4), 649–676, doi:

10.1002/(SICI)1096-9861(19960805)371:4<1649::AID-CNE12>3.0.CO;2-E. [PubMed: 8841916]

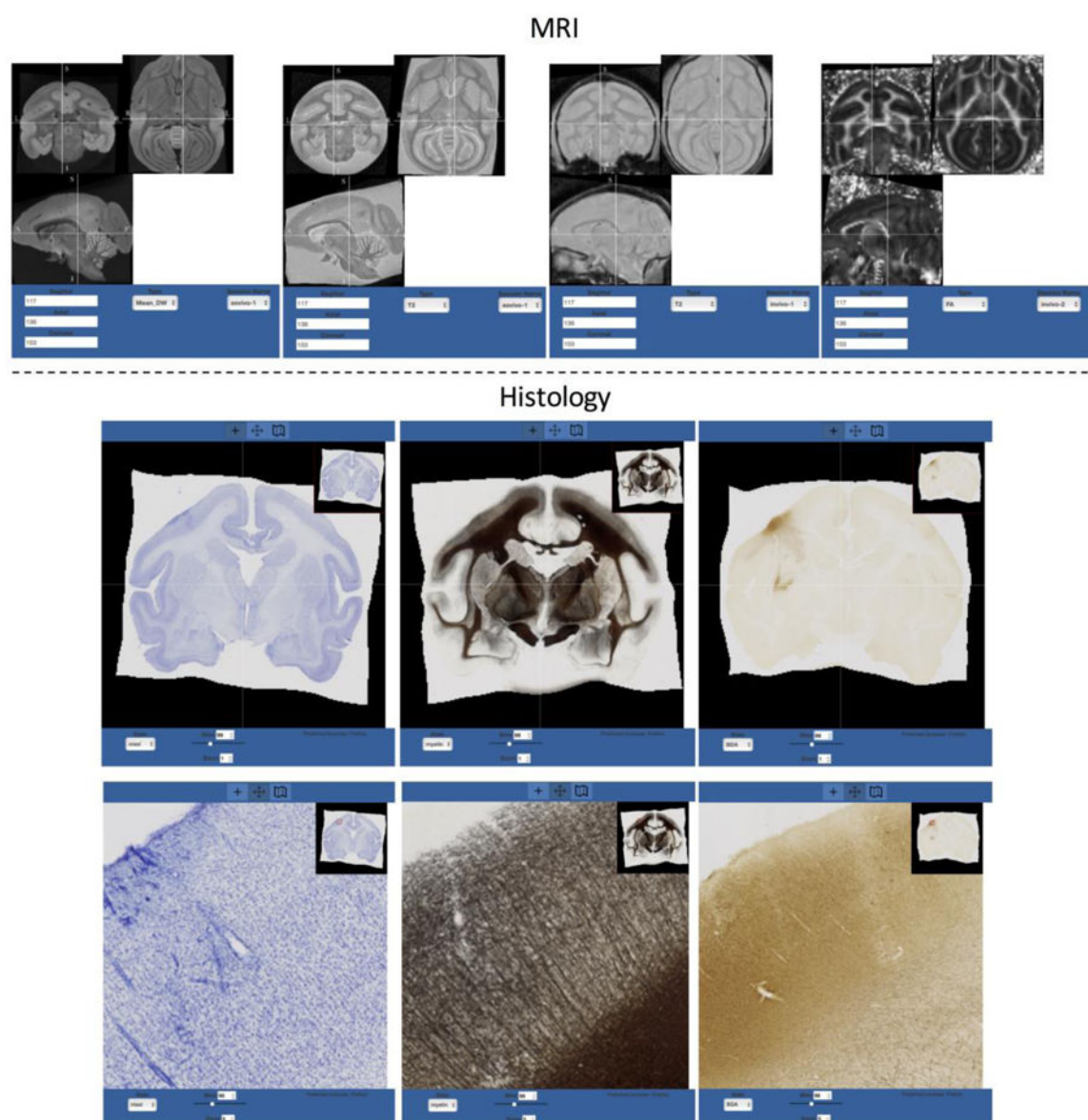
- Reiner A, Veenman CL, Medina L, Jiao Y, Del Mar N, & Honig MG (2000). Pathway tracing using biotinylated dextran amines. *J Neurosci Methods*, 103(1), 23–37. [PubMed: 11074093]
- Roe AW, Winberry JE, & Friedman RM (2017). Study of single and multidigit activation in monkey somatosensory cortex using voltage-sensitive dye imaging. *Neurophotonics*, 4(3), 031219, doi: 10.1117/1.NPh.4.3.031219. [PubMed: 28573156]
- Rohde GK, Aldroubi A, & Dawant BM (2003). The adaptive bases algorithm for intensity-based nonrigid image registration. *IEEE Trans Med Imaging*, 22(11), 1470–1479, doi:10.1109/tmi.2003.819299. [PubMed: 14606680]
- Schilling K, Janve V, Gao Y, Stepniewska I, Landman BA, & Anderson AW (2016). Comparison of 3D orientation distribution functions measured with confocal microscopy and diffusion MRI. *Neuroimage*, 129, 185–197, doi:10.1016/j.neuroimage.2016.01.022. [PubMed: 26804781]
- Schilling KG, Gao Y, Stepniewska I, Wu TL, Wang F, Landman BA, et al. (2017). The VALiDATE29 MRI Based Multi-Channel Atlas of the Squirrel Monkey Brain. *Neuroinformatics*, doi:10.1007/s12021-017-9334-0.
- Schmahmann JD, & Pandya D (2009). *Fiber pathways of the brain*: OUP USA.
- Secci ME, Auber A, Panlilio LV, Redhi GH, Thorndike EB, Schindler CW, et al. (2017). Attenuating Nicotine Reinforcement and Relapse by Enhancing Endogenous Brain Levels of Kynurenic Acid in Rats and Squirrel Monkeys. *Neuropsychopharmacology*, 42(8), 1619–1629, doi:10.1038/npp.2017.21. [PubMed: 28139681]
- Stepniewska I, Preuss TM, & Kaas JH (1993). Architectonics, somatotopic organization, and ipsilateral cortical connections of the primary motor area (M1) of owl monkeys. *J Comp Neurol*, 330(2), 238–271, doi:10.1002/cne.903300207. [PubMed: 7684050]
- Sun P, Parvathaneni P, Schilling KG, Gao Y, Janve V, Anderson A, et al. (2015). Integrating histology and MRI in the first digital brain of common squirrel monkey, *Saimiri sciureus*. *Proc SPIE Int Soc Opt Eng*, 9417, doi:10.1117/12.2081443.
- Sunkin SM, Ng L, Lau C, Dolbeare T, Gilbert TL, Thompson CL, et al. (2013). Allen Brain Atlas: an integrated spatio-temporal portal for exploring the central nervous system. *Nucleic Acids Res*, 41 (Database issue), D996–D1008, doi:10.1093/nar/gks1042. [PubMed: 23193282]
- Toga AW, Ambach KL, & Schluender S (1994). High-resolution anatomy from in situ human brain. *Neuroimage*, 1(4), 334–344, doi:10.1006/nimg.1994.1018. [PubMed: 9343583]
- Toga AW, Samiaie M, & Payne BA (1989). Digital rat brain: a computerized atlas. *Brain Res Bull*, 22(2), 323–333. [PubMed: 2706541]
- Tournier JD, Calamante F, & Connelly A (2012). MRtrix: Diffusion tractography in crossing fiber regions. *International journal of imaging systems and technology*, 22(1), 53–66, doi:10.1002/ima.22005.
- Uno Y, Uehara S, & Yamazaki H (2016). Utility of non-human primates in drug development: Comparison of non-human primate and human drug-metabolizing cytochrome P450 enzymes. *Biochem Pharmacol*, 121, 1–7, doi:10.1016/j.bcp.2016.06.008. [PubMed: 27318253]
- Wang Z, Chen LM, Nagyessy L, Friedman RM, Mishra A, Gore JC, et al. (2013). The relationship of anatomical and functional connectivity to resting-state connectivity in primate somatosensory cortex. *Neuron*, 78(6), 1116–1126, doi:10.1016/j.neuron.2013.04.023. [PubMed: 23791200]
- Woodward A, Hashikawa T, Maeda M, Kaneko T, Hikishima K, Iriki A, et al. (2018). The Brain/ MINDS 3D digital marmoset brain atlas. *Sci Data*, 5, 180009, doi:10.1038/sdata.2018.9. [PubMed: 29437168]
- Wu TL, Wang F, Anderson AW, Chen LM, Ding Z, & Gore JC (2016). Effects of anesthesia on resting state BOLD signals in white matter of non-human primates. *Magn Reson Imaging*, 34(9), 1235–1241, doi:10.1016/j.mri.2016.07.001. [PubMed: 27451405]
- Yeh FC, Verstynen TD, Wang Y, Fernandez-Miranda JC, & Tseng WY (2013). Deterministic diffusion fiber tracking improved by quantitative anisotropy. *PLoS One*, 8(11), e80713, doi:10.1371/journal.pone.0080713. [PubMed: 24348913]



**Figure 1.**  
Atlas data acquisition pipeline.



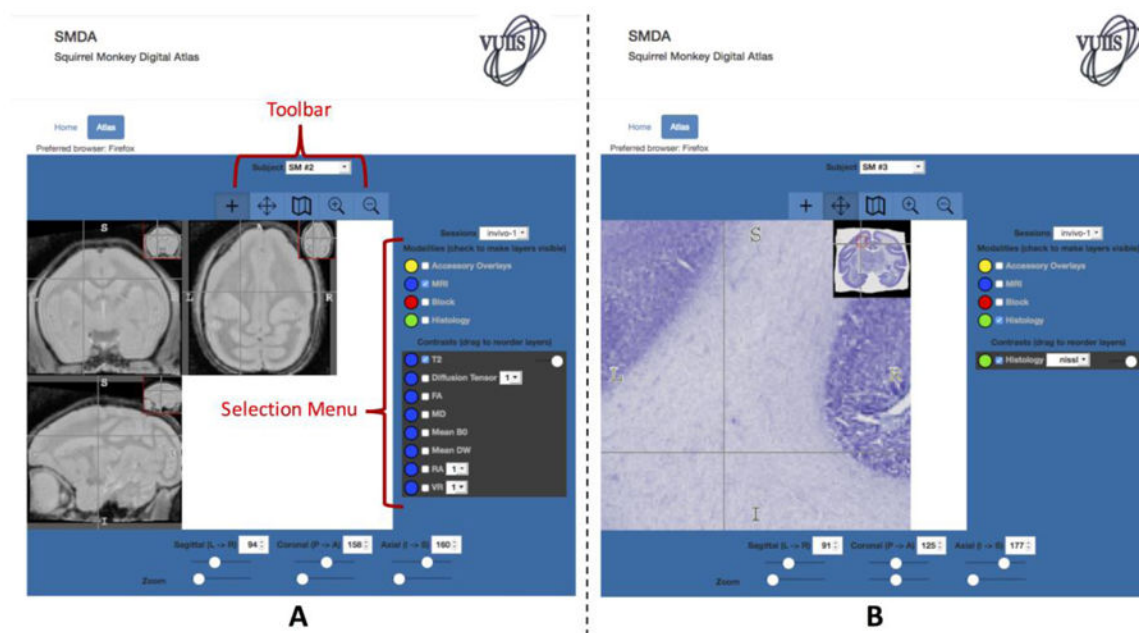
**Figure 2.** Atlas framework. Registration from one space to another allows comparisons across modalities.



**Figure 3.**

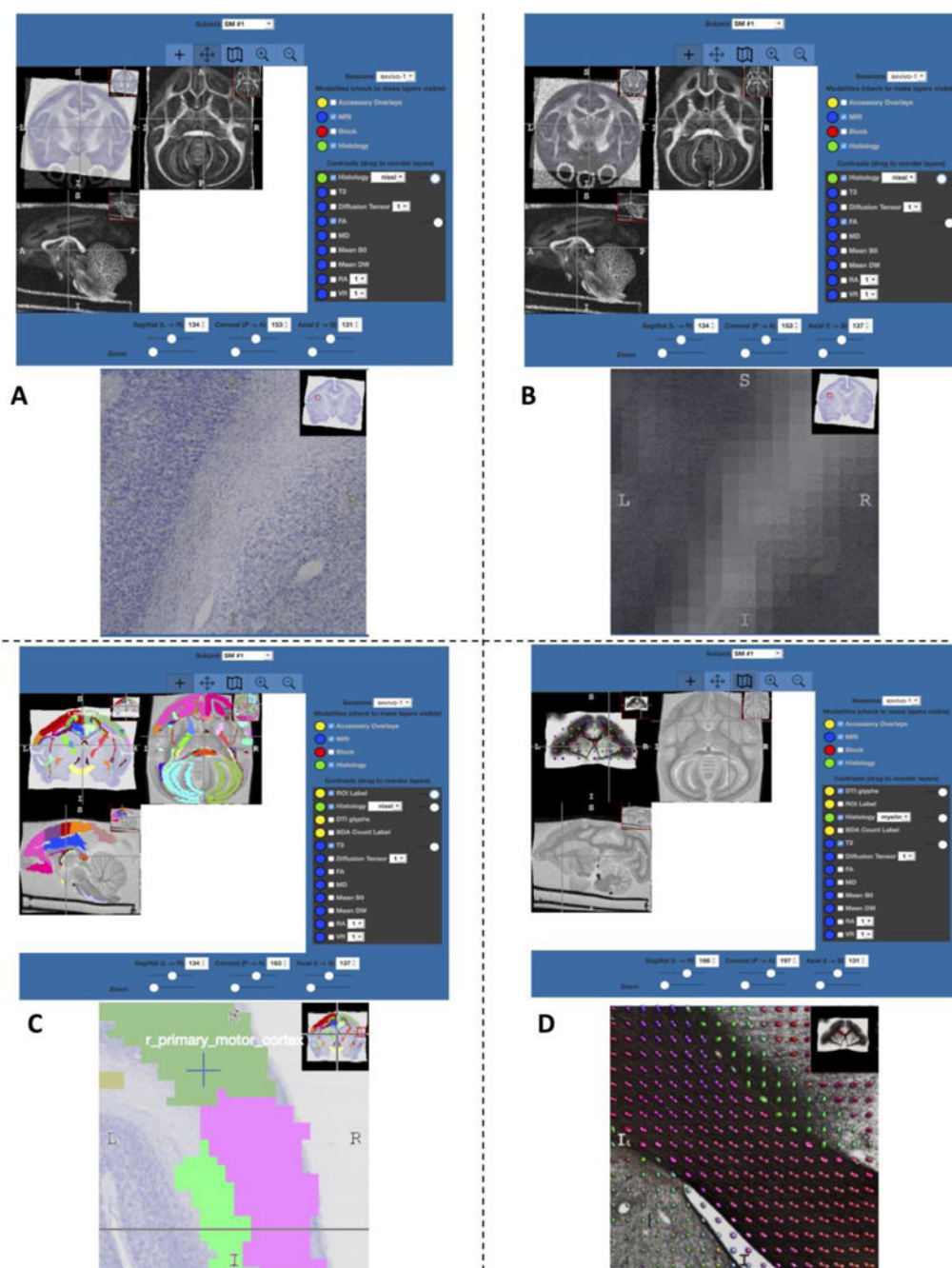
Atlas Contents. For all subjects and sessions, the atlas contains both MRI (top) and histological (bottom) data. Here, selected MRI contrasts are shown for a single subject for the same coronal, sagittal, and axial slices. Similarly, histological contrasts of Nissl, myelin, and BDA stains are shown for the same single subject.





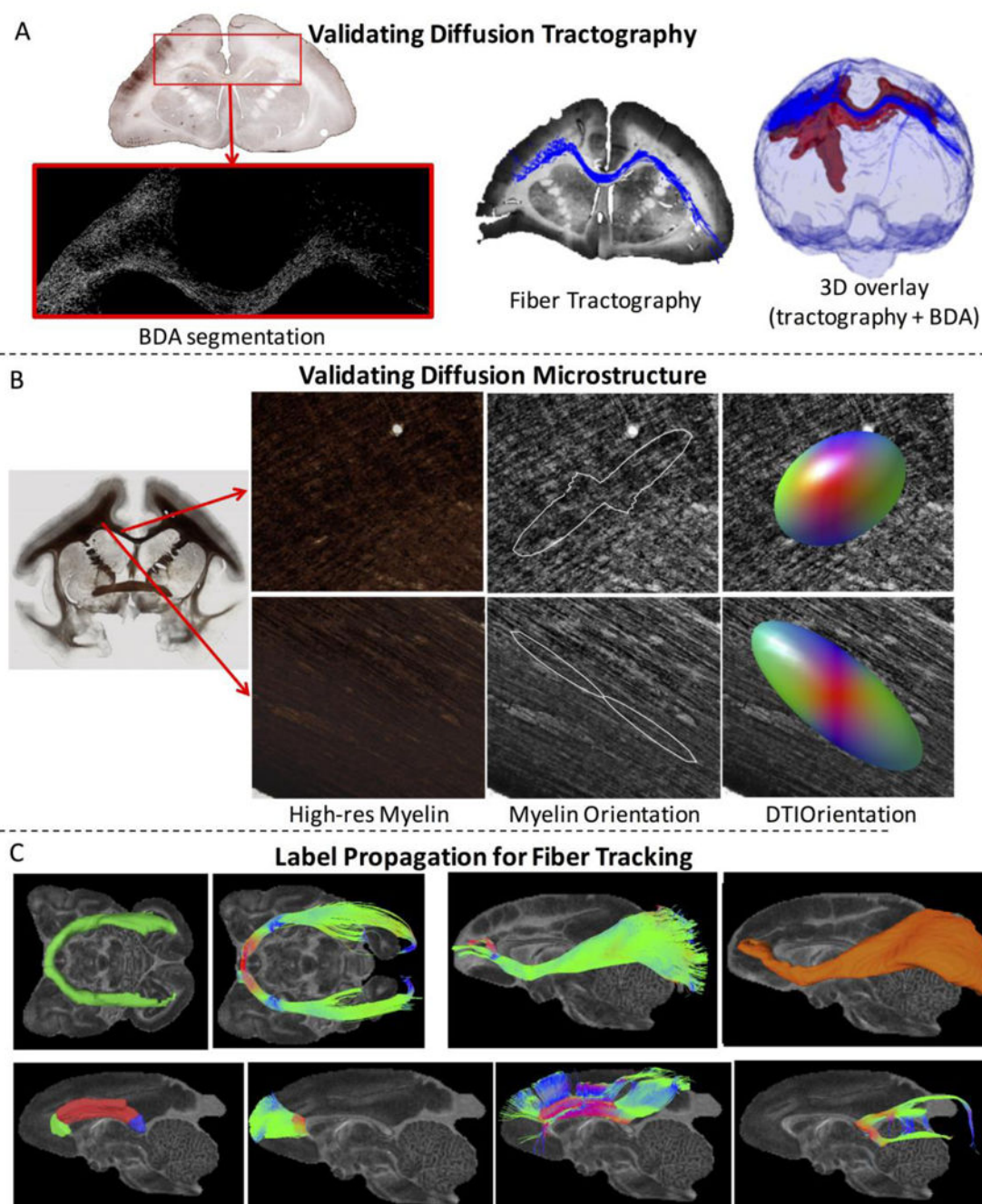
**Figure 4.** Atlas interface and functionality. The toolbars, menus, and display associated with MRI (A) and histology (B) modalities are shown.





**Figure 5.**

Image overlays. Overlays of Nissl-stained histology and FA maps from MRI (A and B) at low (top) and high (bottom) zoom levels. Overlays of ROI labels (C) and DTI glyphs (D) at low (top) and high (bottom) zoom levels. Alpha levels can be adjusted for each contrast/overlay independently.

**Figure 6.**

Atlas applications. The data in this atlas can be used for validation of diffusion tractography (A) by comparing BDA stains (red in the overlay) to fiber tractography (blue) algorithms; validating diffusion microstructure measurements (B) through comparisons with myelin or Nissl stained sections; and (C) label propagation to new subjects for fiber tracking or region of interest delineation. Here, fiber tractography for the Optic Tract (top left), inferior occipito-frontal fasciculus (top right) and genu, body, and splenium of the corpus callosum (bottom) are shown. We note that, in these examples, the BDA (A), myelin (B), and labels

(C) are directly from our atlas data, while the tractography (A and C) and orientation maps (B) are calculated results not currently in the atlas, but easily derived from atlas data.

Author Manuscript

Author Manuscript

Author Manuscript

Author Manuscript

**Table 1.**

Neuroanatomical labels included in the atlas. 18 Gray Matter and 57 White Matter labels, as well as 6 additional regions of interest, are delineated in the atlas.

Gray Matter			
1	L Prefrontal Cortex	2	R Prefrontal Cortex
3	L Primary Motor Cortex	4	R Primary Motor Cortex
5	L Supplementary Motor Area	6	R Supplementary Motor Area
7	L Parietal Ventral Area	8	R Parietal Ventral Area
9	L Cingulate Cortex	10	R Cingulate Cortex
11	L Anterior Parietal Cortex	12	R Anterior Parietal Cortex
13	L Posterior Parietal Cortex	14	R Posterior Parietal Cortex
15	L Premotor Cortex	16	R Premotor Cortex
17	L Primary Visual Cortex	18	R Primary Visual Cortex
White Matter			
19	Body of Corpus Callosum	20	Genu of Corpus Callosum
21	Splenium of Corpus Callosum	22	<i>Label Not Used</i>
23	L Anterior Limb Internal Capsule	24	R Anterior Limb Internal Capsule
25	L Genu of Internal Capsule	26	R Genu of Internal Capsule
27	L Posterior Limb Internal Capsule	28	R Posterior Limb Internal Capsule
29	Fornix	30	<i>L/R Fornix Not Seperated</i>
31	Posterior Commissure	32	Anterior Commissure
33	L External Capsule	34	R External Capsule
35	L Externe Capsule	36	R Externe Capsule
37	L Cingulum	38	R Cingulum
39	L Uncinate Fasciculus	40	R Uncinate Fasciculus
41	Optic Tract + Optic Radiation	42	<i>L/R Optic Tracts Not Seperated</i>
43	L Superior Longitudinal Fasciculus I	44	R Superior Longitudinal Fasciculus I
45	L Superior Longitudinal Fasciculus II	46	R Superior Longitudinal Fasciculus II
47	L Superior Longitudinal Fasciculus III	48	R Superior Longitudinal Fasciculus III
49	L Fronto Occipital Fasciculus	50	R Fronto Occipital Fasciculus
51	L Middle Longitudinal Fasciculus	52	R Middle Longitudinal Fasciculus
53	L Inferior Longitudinal Fasiculus I	54	R Inferior Longitudinal Fasciculus I
55	L Forceps Minor	56	R Forceps Minor
57	L Medullary Stria of Thalamus	58	R Medullary Stria of Thalamus
59	L Superior Corona Radiata	60	R Superior Corona Radiata
61	L Corticospinal Tract	62	R Corticospinal Tract
63	L Cerebellar Peduncle	64	R Cerebellar Peduncle
65	L Inferior Fronto Occipital Fasciculus	66	R Inferior Fronto Occipital Fasciculus
67	L Forceps Major	68	R Forceps Major
69	L Extension of Corpus Callosum Body	70	R Extension of Corpus Callosum Body

71	L Anterior Corona Radiata	72	R Anterior Corona Radiata
73	L Inferior Longitudinal Fasciculus II	74	R Inferior Longitudinal Fasciculus II
75	L Dorsal Posterior Corona Radiata	76	R Dorsal Posterior Corona Radiata
77	L Posterior Corona Radiata	78	R Posterior Corona Radiata
<b>Other</b>			
81	Third Ventricle	82	Fourth Ventricle
83	L Lateral Ventricles (One and Two)	84	R Lateral Ventricles (One and Two)
85	L Claustrum	86	R Claustrum